Emergent Materials
https://doi.org/10.1007/s42247-025-01215-4

ORIGINAL ARTICLE

Physical properties comparison of two-dimensional materials: MXene and graphene oxide

Michal Procházka[1] · **Yaryna Soyka**[1] · **Anastasiia Stepura**[1] · **Nikola Bugárová**[1] · **Peter Machata**[1] · **Matej Mičušík**[1] · **Gediminas Monastyreckis**[2] · **Daiva Zeleniakiene**[2] · **Andrey Aniskevich**[3] · **Mária Omastová**[1]

Received: 25 March 2025 / Accepted: 27 July 2025

Abstract

Two-dimensional (2D) nanomaterials are promising for many different applications. Therefore, detailed characterization and knowledge of their properties are needed. This work focused on graphene oxide (GO) and a new 2D nanomaterial, MXene, type $Ti_3C_2T_x$. The spray coating method was used to create thin GO and MXene films on a glass substrate. Their composition was characterized by X-ray photoelectron spectroscopy. Scanning probe microscopy (SPM) imaging and surface free energy calculation confirmed the homogenous coating of the substrate. The mechanical properties of the prepared films were measured by nanoindentation. The elastic modulus was independent of the film thickness; it was approximately 89 GPa for the MXene samples and approximately 100 GPa for the GO samples. Lower hardness values were determined for thicker films: 10.5 GPa for 5-layer MXene vs. 7.5 GPa for 10-layer MXene and 13.0 GPa for 5-layer GO vs. 9.8 GPa for 10-layer GO. Contact angle measurements and surface energy calculations were performed for all prepared films with 5 or 10 layers. MXenes oxidize on air over time, and the highly conductive $Ti_3C_2T_x$ structure changes to less conductive titanium oxides. The aging of MXene was studied by monitoring the MXene film conductivity within two months, which showed a decrease, but the 10-layer films were more stable than the thinner 5-layer films.

Keywords $Ti_3C_2T_x$ MXene · Graphene oxide · Nanoindentation · Surface properties · Mechanical properties

1 Introduction

Two-dimensional (2D) materials have attracted global interest due to their exceptional electrical, thermal, and mechanical properties. Their mechanical characteristics are especially critical for applications such as 2D nanodevices [1].

Graphene oxide (GO), an oxidized graphene derivative, was first synthesized by Benjamin Brody in 1859 [2]. Modern GO synthesis leverages graphite's ability to intercalate

---

✉ Michal Procházka
michal.prochazka@savba.sk

✉ Matej Mičušík
matej.micusik@savba.sk

Yaryna Soyka
yaryna.soyka@savba.sk

Anastasiia Stepura
anastasiia.stepura@savba.sk

Nikola Bugárová
nikola.bugarova@savba.sk

Peter Machata
peter.machata@savba.sk

Gediminas Monastyreckis
gediminas.monastyreckis@ktu.lt

Daiva Zeleniakiene
daiva.zeleniakiene@ktu.lt

Andrey Aniskevich
andrey.aniskevich@pmi.lv

Mária Omastová
maria.omastova@savba.sk

[1] Polymer Institute SAS, Dúbravská cesta 9, Bratislava 845 41, Slovakia

[2] Department of Mechanical Engineering, Kaunas University of Technology, Studentu st. 56, Kaunas 51424, Lithuania

[3] Institute for Mechanics of Materials, University of Latvia, Riga LV-1004, Latvia

atoms, expanding interlayer distances and enabling chemical oxidation into single-layer GO. The widely used Hummers-Offeman method employs H_2SO_4, $NaNO_3$, and $KMnO_4$, producing GO suspensions with high yield and efficiency [3].

The oxygen atoms in GO are located on the basal planes and sheet edges. Its structure has been extensively studied using techniques such as transmission electron microscopy (TEM) [4, 5], scanning electron microscopy (SEM) [6], X-ray photoelectron spectroscopy (XPS) [7] and many others. These analyses revealed an uneven oxygen distribution, with a higher concentration on sheet edges (Fig. 1). This structure significantly influences GO's properties: oxygen atoms enhance hydrophilicity, alter electrical conductivity, and increase chemical reactivity. These features make GO useful in sensors, catalysts, and drug delivery systems. In many applications, it serves as a filler in composites, requiring excellent mechanical performance. Therefore, understanding the mechanical behavior of isolated GO layers is essential for such use. Alejandra Huitrón Segovia et al. [8] reviewed several studies and reported a wide range of elastic moduli for GO papers and films from 6 to 42 GPa, and up to 200 GPa for few-layer films. Mechanical properties also depend on surface roughness, chemical composition, and the type of functional groups present. GO is electrically insulating due to a disrupted sp^2 network [9, 10]. One of its most promising applications is in polymer nanocomposites [9].

MXenes, a newer class of 2D materials discovered in 2011 [11] have rapidly expanded to over 30 synthesized variants. The first MXene, Ti_3C_2, was obtained by etching Ti_3AlC_2 with hydrofluoric acid, later improved via the MILD method using LiF/HCl [12]. Although MXenes are still relatively new materials, only a few publications have focused on experimental studies of their mechanical properties. These publications are focused on the mechanical properties of a single sheet of MXene, where the reported Young's modulus of a single layer of $Ti_3C_2T_x$ is approximately 330 GPa [13]. The mechanical properties of MXenes depend on the thickness of single sheets, which increases with their chemical composition. MXene $Ti_3C_2T_x$ is made up of a titanium carbide (Ti_3C_2) layer with a hexagonal lattice and surface functional groups (T_x) that can be oxygen (O), fluorine (F), or hydroxyl (OH). The Ti_3C_2 layer is composed of three layers of titanium atoms and two layers of carbon atoms, and the T_x functional groups are bonded to the Ti_3C_2 layer through covalent bonds (see Fig. 2). The structure of MXene $Ti_3C_2T_x$ has been studied extensively using a variety of techniques, including transmission electron microscopy (TEM) [14, 15], small-angle neutron scattering (SANS) [16], and X-ray photoelectron spectroscopy (XPS) [17]. These studies have revealed that the $Ti_3C_2T_x$ layer is typically approximately 1 nm thick, and the T_x functional groups are typically approximately 0.5 nm thick.

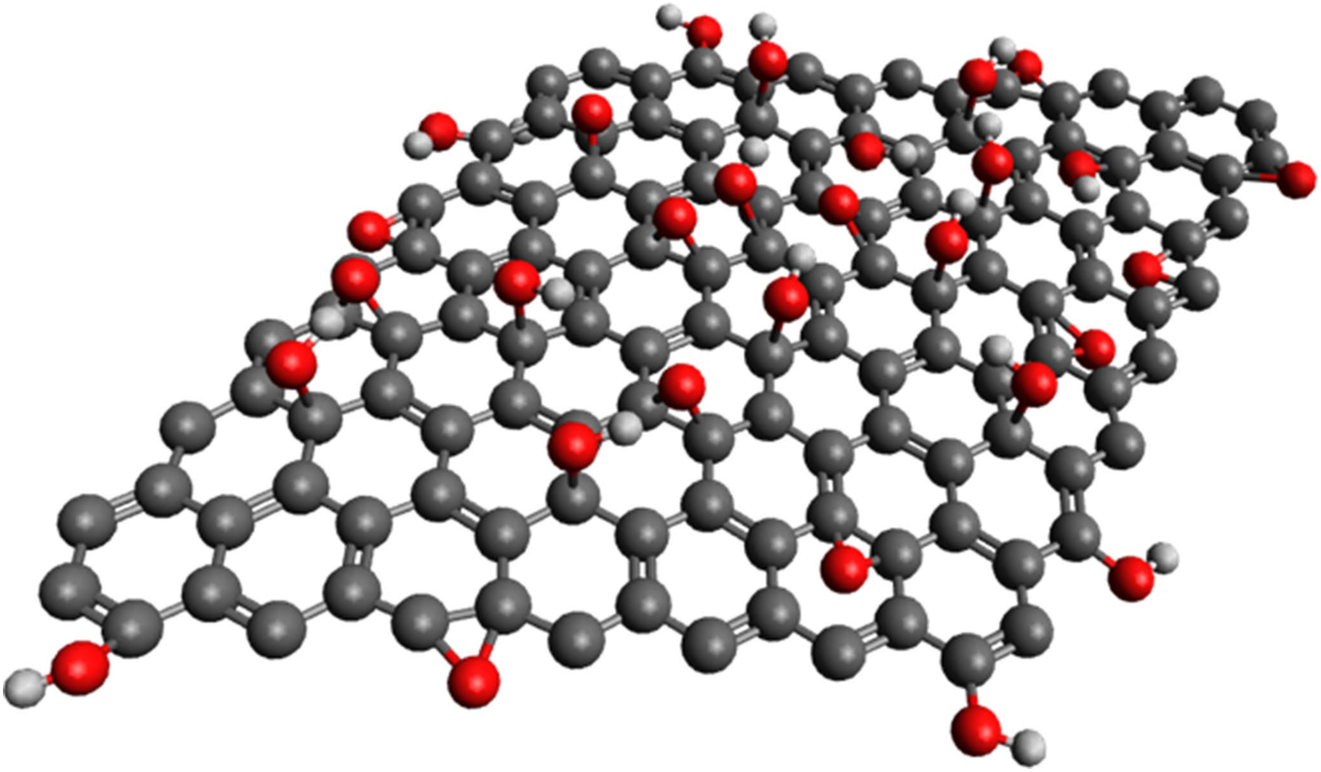

Fig. 1 Lerf–Klinowski model of GO with groups (carboxyl, carbonyl, ester, etc.)

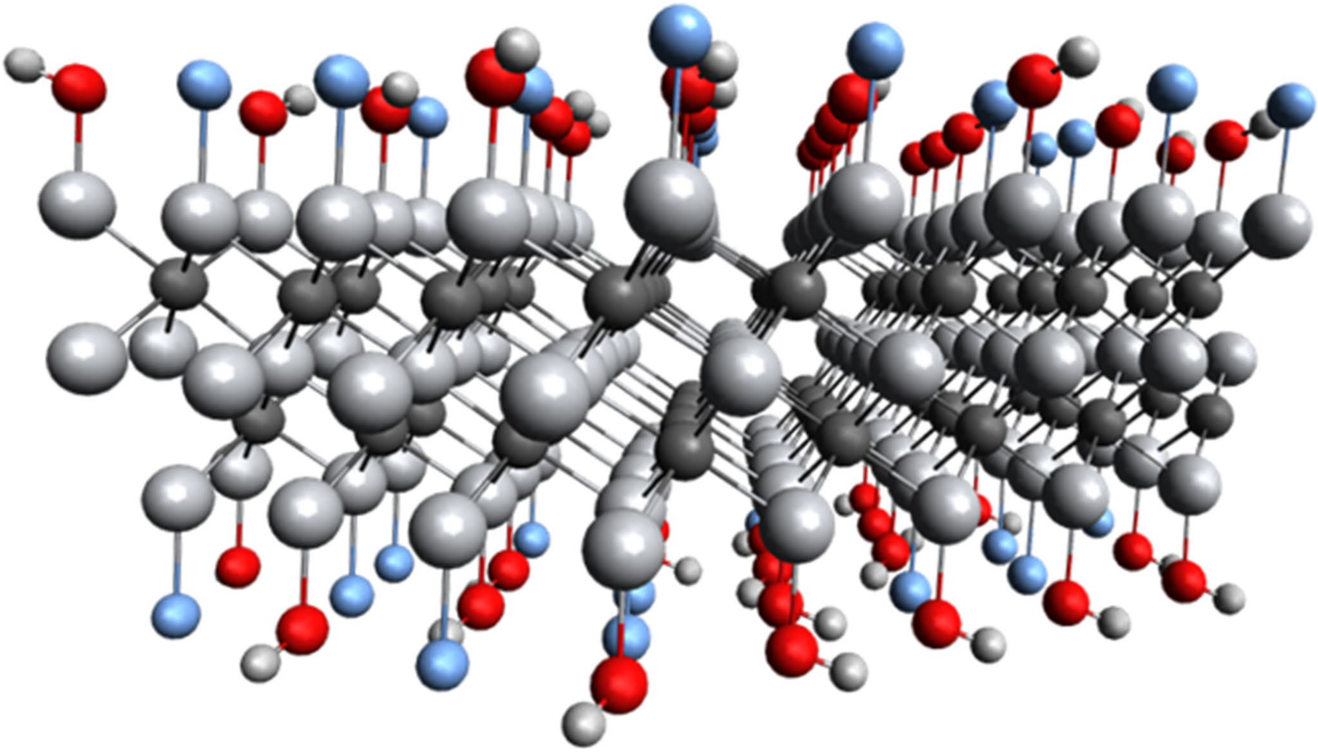

Fig. 2 Schematic diagram of the atomic structure of MXene: $Ti_3C_2T_x$

Simulations of free-standing films revealed that the mechanical behavior of MXene films is predominantly influenced by their interlaminar shear strength and in-plane stiffness [18]. MXenes are one of the most conductive nanomaterials, reaching almost metallic conductivity. The conductivity of monolayer $Ti_3C_2T_x$ MXene up to 11 000 S/cm was reported [19]. However, MXene films containing many layers can exhibit lower conductivities, even by several orders of magnitude [20]. This phenomenon is attributed to contact resistance between flakes, which cannot be eliminated. In addition, the MXene surface can be chemically modified by different functional groups without a significant loss of conductivity. These properties predetermine the suitability of MXenes for use in various applications.

MXenes are new materials with impressive properties, primarily electrical and mechanical. In the future, they could replace graphene and GO in many applications. MXenes and graphene particles are also used for polymeric composite preparation. Tarasovs and Aniskevich [21] studied the effect of clusterization on the effective properties of a composite material using the representative volume element (RVE) method.

Although monolayers are well-studied [13, 22–24] direct comparisons of spray-coated $Ti_3C_2T_x$ MXene and GO films remain rare. These sprayed films differ structurally from monolayers and their mechanical properties depend on layer alignment, thickness, and substrate interactions. Spray coating supports nanoflake alignment [25], though less orderly than vacuum filtration.

The differences in mechanical properties between sprayed and vacuum-filtered films are primarily due to the differences in their layer thickness. Sprayed films are typically thinner than vacuum-filtered films, which results in weaker interlayer interactions [26, 27].

The comparison of mechanical properties between sprayed and vacuum-filtered $Ti_3C_2T_x$ MXene and graphene oxide films is important for understanding the impact of fabrication methods on material properties. Spray coating offers several advantages over vacuum filtration, including scalability, cost-effectiveness, and the ability to produce patterned films. And the thinner layer thickness of sprayed films can lead to higher mechanical properties.

Further research is warranted to systematically investigate the mechanical properties of sprayed $Ti_3C_2T_x$ MXene and graphene oxide films across a range of parameters, including film thickness, morphology, and additive compositions. This knowledge will pave the way for the development of advanced materials with tailored mechanical properties for applications in electronics, energy storage, and catalysis.

In this study, for the first time, the physical properties of $Ti_3C_2T_x$ MXene and GO films prepared using the same spray coating method on glass substrates are compared, addressing a gap in current knowledge. This technique enables coating of large substrate areas with uniform, thin, and smooth films. Spray coating offers several advantages over traditional methods, including high deposition efficiency and rate, minimal masking, and the ability to form dense coatings with strong substrate adhesion. Cold spray eliminates the need for grit blasting, reducing substrate damage, and provides coatings with minimal thermal input, high bond strength, compressive residual stress, and excellent corrosion resistance, strength, and conductivity. It avoids phase changes, oxidation, and grain growth. The resulting films exhibit good long-term stability, making them suitable for various demanding applications [28] Cold spray is a valuable coating method for a variety of applications, including aerospace, automotive, manufacturing, and medical industries [29].

The chemical structure of all samples was analyzed using X-ray photoelectron spectroscopy. Surface morphology and homogeneity were assessed via scanning probe microscopy (SPM). Wettability and surface free energy of the hydrophilic 2D films were evaluated through contact angle hysteresis. Mechanical properties were determined by nanoindentation, enabling a consistent comparison of both materials. $Ti_3C_2T_x$ MXene film conductivity was monitored over two months to assess film aging at different thicknesses.

2 Materials and methods

$Ti_3C_2T_x$ MXene was prepared by etching MAX phase Ti_3AlC_2 (MRC, Ukraine) using the modified MILD method [30]. Briefly, the MAX phase was slowly added to the HCl/LiF mixture and stirred overnight to remove the Al layer from the structure. The prepared MXene was next delaminated with LiF and centrifuged to obtain a single layer MXene solution with a concentration of 2.58 mg/ml [31].

GO was synthesized from bulk graphite (particle size of 5 µm) using a modified Hummers and Offeman method [3]. The resulting solution was purified and monolayer GO was selected through multiple centrifugation and sonication steps, achieving a final concentration of 3.00 mg/ml.

Films of 2D nanomaterials were prepared by spray coating onto a cleaned glass substrate. All glass substrates were cleaned in an ultrasonic bath following the procedure: 5 min in DI water with detergent, 5 min in pure DI water, and 5 min in ethanol. Next, the samples were dried in air. Before spraying, glass plates were treated by air plasma in a plasma generator at 40 kHz and 100 W under an air pressure of approximately 0.2 mbar. A water suspension of $Ti_3C_2T_x$ MXene or GO was sprayed by hand from a distance of approximately 20 cm using a spray gun with airflow at a pressure of 1 bar. After spraying one layer, the samples were dried in an oven at 35 °C for 30 min, and the next layer was sprayed. Five-layer and ten-layer films were prepared and characterized.

GO was coated on a glass substrate by the same procedure as that used for MXene. GO contains various polar functional groups similar to $Ti_3C_2T_x$ MXene, creating films with similar bonding between their single sheets.

The term “layers” in this manuscript refers to the number of spray-applied layers, not to the number of MXene of GO monolayers.

The mechanical properties of the prepared films were evaluated using a Nanoindenter TI 750 Ubi (Hysitron, USA) with a Berkovich diamond probe with a tip radius of approximately 150 nm was used. An area of size 60×60 μm^2 was scanned at a rate of 0.25 Hz and a setpoint of 2 µN. Temperatures during all experiments ranged from 22 to 25 °C, with relative humidity between 29.2 and 33.6 RH%. This technique also enabled surface topography analysis through its Scanning Probe Microscopy (SPM) mode. SPM scans were visualized and analyzed by the software Gwyddion 2.53.

Nanoindentation helps to obtain values required for the study of wetting behavior. A Young contact angle is necessary for further surface energy calculation using the most stable contact angle obtained by contact angle measurement. For calculation of the Young contact angle, it is necessary to know the roughness ratio r, which is defined as the ratio between the real area (A_{real}) and the geometrical area (A_{geom}). These values can be obtained from nanoindentation measurement reports.

$$r = \frac{A_{real}}{A_{geom}} \tag{1}$$

In Gwyddion are computed by simple triangulation and shown in Hybrid statistical values as the “Projected surface area” $A_{\mathrm{geom}} = 3600\ \mu m^2$ for all samples and the “Surface area” A_{real} calculated for each sample.

The morphology of the 2D particles was characterized by an EVO® 40 Series scanning electron microscope (JEOL, Japan). The XPS signals were recorded using a K-Alpha XPS system (Thermo Fisher Scientific, UK), equipped with a microfocused, monochromatic Al K-α X-ray source (1486.68 eV) and an X-ray beam size of 400 µm. Spectra were acquired in constant analyzer energy mode, with a pass energy of 200 eV for surveys and 50 eV for narrow regions. Charge compensation was achieved via the system’s flood gun. Depth profile analysis was conducted with an Ar ion gun at an etching rate of approximately 0.29 nm/s. Data acquisition and processing were performed using Thermo Scientific Avantage software, version 5.9931. Spectral calibration was conducted using an automated routine with internal Au, Ag, and Cu standards provided by the K-Alpha system. Surface compositions (in atomic %) were determined from integrated peak areas of detected atoms and corresponding sensitivity factors.

The electrical properties of the films were characterized using a Four-Point Probe System (Ossila, UK). Contact angle measurements were conducted on an OCA 25 device (Dataphysics, Germany), utilizing a syringe needle with an outer diameter of 0.31 mm and an inner diameter of 0.16 mm. Advancing and receding contact angles were measured by varying the drop volume at a constant volumetric flow rate using a motorized syringe. An ellipsoid method was used to fit the experimental data. Laboratory humidity was maintained between 20 and 30%, and experiments were performed at temperatures of 23–25 °C. For contact angle measurements, diiodomethane (CH_2I_2, purity 99%) was sourced from Sigma-Aldrich Co. (USA), ethyl anthranilate (purity > 99%) was provided by Tokyo Chemical Industry Co., Ltd. (Japan), and ultrapure water (18.2 MΩ·cm) was obtained from an AquaPro ultrapure water production system.

3 Results and discussion

Solutions of 2D nanomaterials, $Ti_3C_2T_x$ MXene and GO, were used for the preparation of compact films using spray coating on a glass substrate. For the comparison of physical properties, GO was chosen, not graphene, because a water-soluble material is needed for the spray coating onto the glass substrate, and graphene is hydrophobic and not water-soluble.

3.1 X-ray photoelectron spectroscopy investigation

The chemical composition of the prepared structures was checked and compared using X-ray photoelectron spectroscopy (XPS, Figure S6). Table 1 summarizes the apparent surface chemical composition of the $Ti_3C_2T_x$ MXene 5-layer film (MX-5 L) and 10-layer film (MX-10 L), graphene oxides in the form of a 5-layer film (GO-5 L), and GO as a 10-layer film as determined by XPS.

$Ti_3C_2T_x$ MXene films showed only minor oxidation at the Ti structure, and typical peaks for Ti_3C_2 were detected (Ti2p at ~455.2 eV, see Fig. 3A). Signals of Ti^{2+} at ~456.1 eV (labeled as "Ti^{2+} ") and Ti^{3+} at ~456.9 eV (labeled as "Ti^{3+}") on the surface in addition to some oxidation (C-Ti-O_x and some suboxides TiO_x) might also be correlated to binding with fluorine, which is also present on the surface.

The O1s XPS spectra of the 10-layer MXene film presented in Fig. 3B can be deconvoluted into four components at 529.9 eV, 531.9 eV, 533.7 eV, and 534.9 eV. The most intense peak at 529.9 eV comes from the oxide species and oxygen bonded to titanium. The peaks at 531.9 eV and 533.7 eV come from the presence of oxygen bound to carbon in surface contamination. F1s signal showed the Ti-F termination groups (F1s at ca. 685 eV, Fig. 3D).

The stoichiometry calculated from the XPS results of the five-layer $Ti_3C_2T_x$ MXene sample is $Ti_3C_{1.91}F_{1.07}O_{1.50,}$ and that for the ten-layer sample is $Ti_3C_{1.83}F_{1.18}O_{1.47}$. These results confirm the presence of non-oxidized $Ti_3C_2T_x$ MXene layer with -F and -O termination groups [32].

Figure 3C shows the C1s XPS spectra of 10-layer $Ti_3C_2T_x$ MXene films and reveals three main peaks occurring at

Table 1 Apparent surface chemical composition as determined by XPS

Surface chemical composition (at%)	Samples			
	MXene 5 layer film 5 L-MX	MXene 10 layer film 10-LMX	GO 5 layer film 5 L-GO	GO 10 layer film 10 L-GO
C1s I/II/sp^2/sp^3/CO/C = O/OCO/π- π*	30.9 15.2/1.9/4.4/5.0/2.9/-/1.5/–	35.4 14.3/2.7/6.4/6.3/3.4/-/2.4/–	55.3 –/–/9.0/30.2/7.8/6.9/1.2/0.3	58.5 –/–/11.3/30.6/4.9/10.1/1.4/0.3
O1s ox/C = O/C-O/COC	20.6 8.2/4.3/7.1/1.0	19.2 7.7/4.6/5.6/1.3	12.7 –/3.9/7.7/1.0	11.6 –/4.6/6.1/0.9
Ti2p TiC//Ti^{2+}/Ti^{3+}/Ti^{4+}	29.6 12.2/8.3/6.3/2.8	28.2 11.9/7.9/8.0/0.5	—	—
F1s F^-/TiF/TiF_2/C-F	12.2 0.2/9.6/1.8/0.6	11.6 0.1/9.3/1.6/0.6	—	—
N1s (N^+)	1.9 (0.5)	2.2 (0.6)	6.1 (4.3)	6.2 (4.7)
Cl2p	2.2	2.2	13.7	13.7
Si2p/Zn2p/S2p/Na1s/Cu2p	2.7/-/-/-/-	1.2/-/-/-/-	1.8/7.5/1.1/1.0/0.8	–/8.0/1.1/0.4/0.6

C1s: I, II = carbide

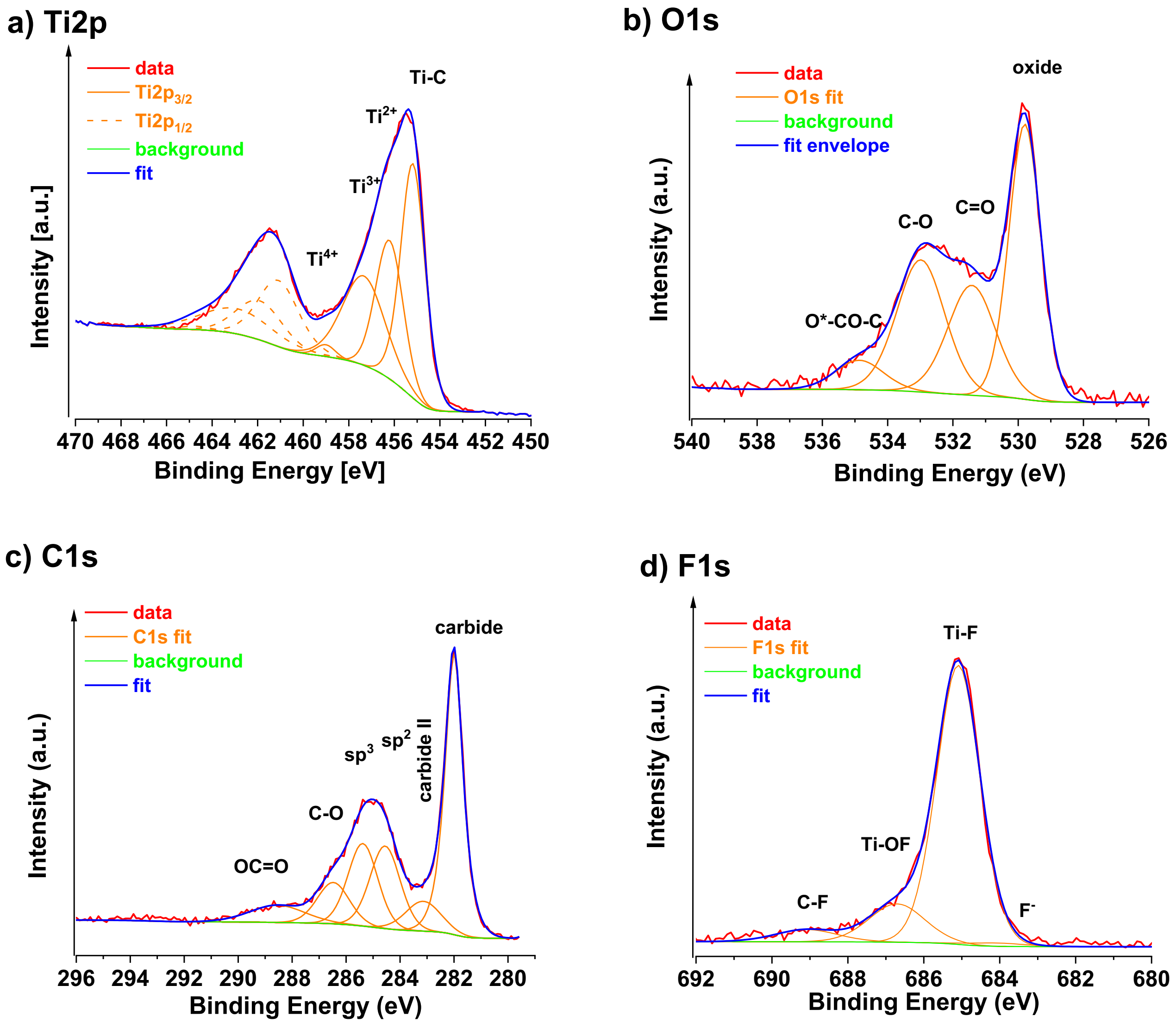

Fig. 3 XPS of 10-layer MXene film (MX-10 L) of (**a**) Ti2p, (**b**) O1s, (**c**) C1s, (**d**) F1s region

≈281.4, ≈284.6, and ≈287.8 eV, which may originate from Ti–C, C–C, and C–O structures, respectively. The presence of C–O may arise from $Ti_3C_2T_x$ MXene oxidation, resulting in the formation of TiO_2 and carbon atom networks or it is consequence of adventitious carbon presence.

The O1s and C1s XPS spectrum of the GO-10 L film is presented in Fig. 4. O1s showed mainly organic oxygen functionalities of C=O and C-O. C1s can be exhaustively described by chemical shifts of carbon–carbon bonds due to sp^2 (signal at ≈284.4 eV) and sp^3 (≈285.0 eV) hybridization and three chemical shifts corresponding to hydroxyl C-O (≈286.1 eV), carbonyl C=O (≈287.3 eV) and carboxyl O=C-O (≈289.2 eV) bonds [33, 34].

3.2 SEM study

SEM images confirmed that using a MILD method for MAX phase etching, single-layer sheets of $Ti_3C_2T_x$ MXenes were prepared. Figure 5a shows a good visible $Ti_3C_2T_x$ MXene single sheet with a diameter of approximately 3 µm, and Fig. 5b shows a GO particle cluster with a diameter of approximately 2 µm.

3.3 Nanoindentation

SPM scans made with nanoindentor shows, then the ten-layer samples (Figs. 6A and C) were smoother than five-layer samples (Figs. 6B and D). The reason may be the ability to self-organize the layers during the successive

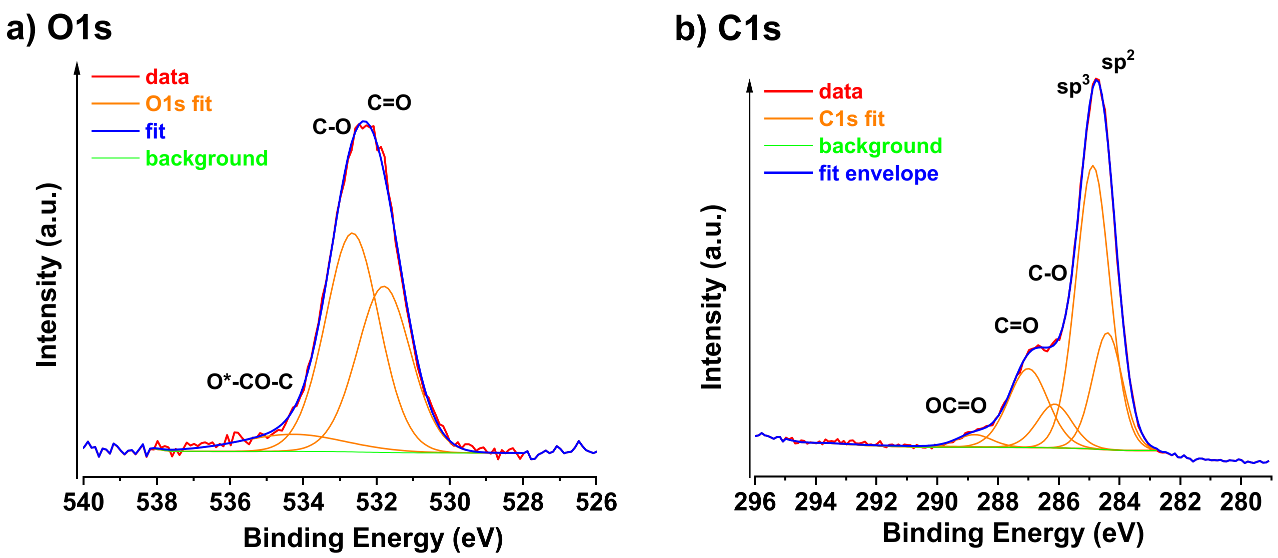

Fig. 4 XPS of 10-layer GO film (GO-10 L) of (**a**) O1s, (**b**) C1s region

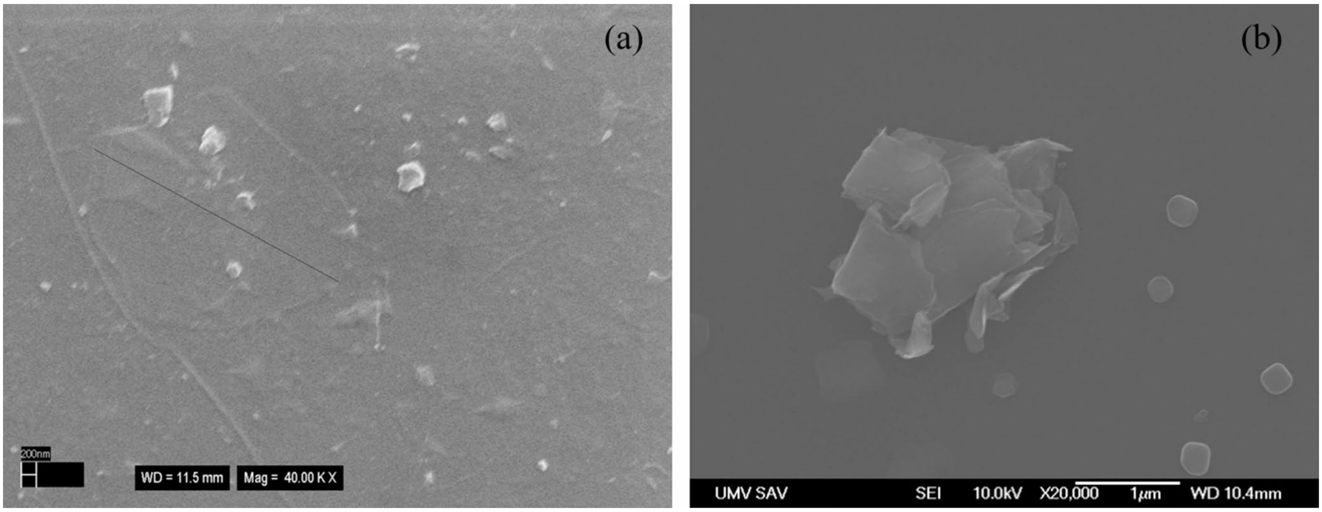

Fig. 5 SEM images of $Ti_3C_2T_x$ MXene single sheets with a diameter of approximately 3 μm on sample MX-5 L (a) and GO particle clusters with a diameter of approximately 2 μm on sample GO-5 L (b)

application, and this evens out the individual irregularities arising on the surface.

The thicknesses of the prepared films were calculated from SPM scans on the interface stage between the films and glass substrate (see Supplementary Information Figure S1). For the 5-layer $Ti_3C_2T_x$ MXene samples, the thickness was calculated from 35.72 to 37.87 nm (average 36.80 nm), and for the 10-layer $Ti_3C_2T_x$ MXene sample, the thickness was calculated from 45.95 to 54.44 nm (average 50.62 nm). For the 5-layer GO sample, the thickness ranged from 15.45 to 34.49 nm (average 23.11 nm), and for the 10-layer GO sample, the calculated thickness ranged from 44.32 to 56.75 nm (average 50.63 nm).

The XRD analysis results are typical for 2D materials as shown in Figure S4. That is a peak at small angles due to the periodic layering of basal monolayers of GO or $Ti_3C_2T_x$ MXene, where the position of the peak indicates the distance between neighbouring monolayers (repeat period). In $Ti_3C_2T_x$ MXenes samples, it takes on a value of 1.51 nm, which is also consistent with the literature [16]. In GO (see Supplementary information Figure S5), it takes on a value of 1.24 to 1.31 nm, which is also in agreement with the literature [35]. By dividing values the thickness of the sprayed films obtained from SPM scans by these values, we would obtain the following numbers of monolayers: for 5-layer MXene samples ~ 24 monolayers, for 10-layer

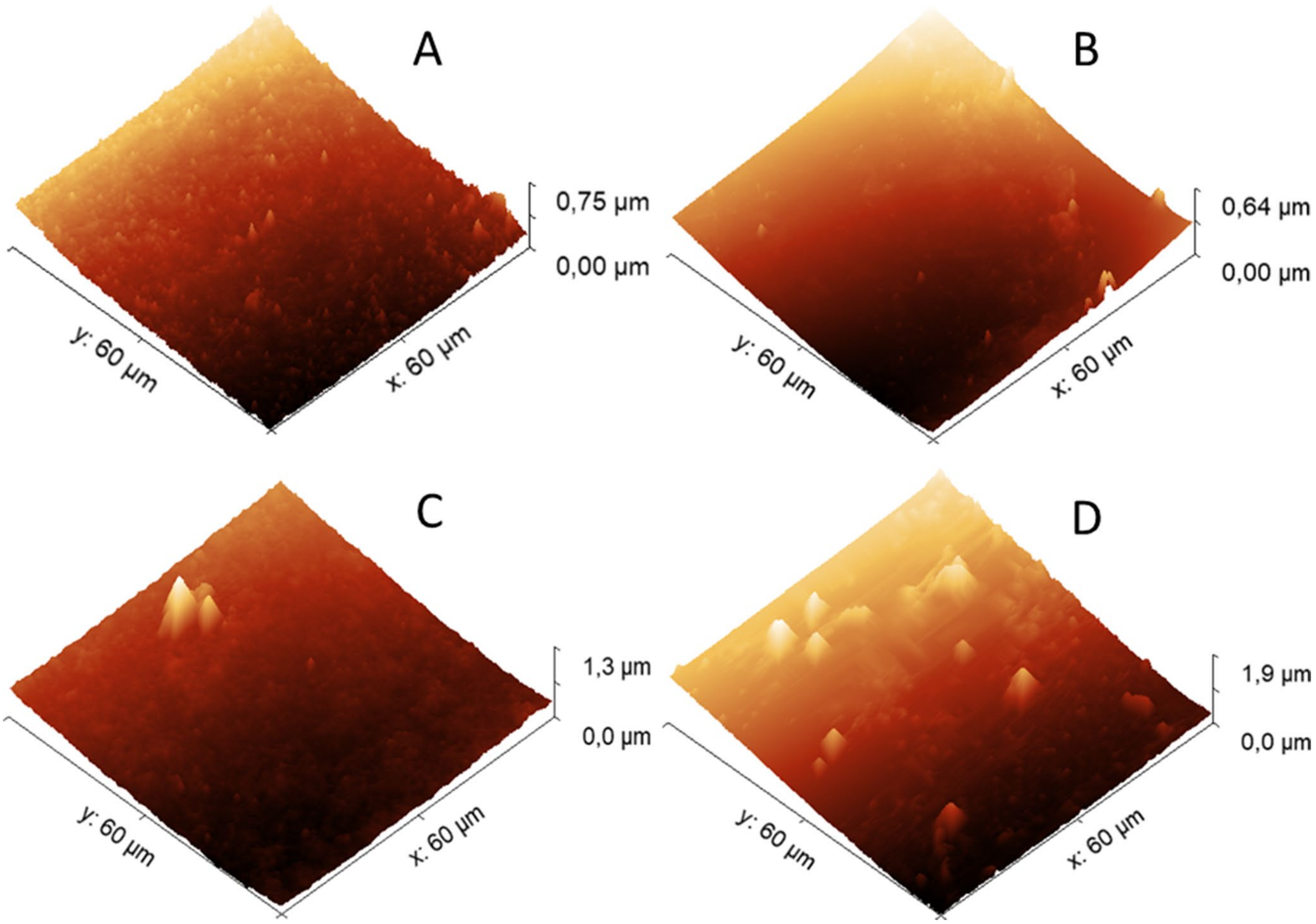

Fig. 6 SPM surface images of (**A**) MX-10 L (A_{real} = 3607,40 µm^2$\boldsymbol{r}$=**1.0020** $\overline{5}$), (**B**) MX-5 L (A_{real} = 3601,75 µm^2$\boldsymbol{r}$=**1.000486** $\overline{1}$), (**C**) GO-10 L (A_{real} = 3610,29 µm^2$\boldsymbol{r}$=**1.002858** $\overline{3}$), and (**D**) GO-5 L (A_{real} = 3625,11 µm^2$\boldsymbol{r}$=**1.006975**)

MXene sample ~ 33 monolayers, for the 5-layer GO sample ~ 18 monolayers, and for the 10-layer GO sample ~ 40 monolayers.

The nanoindentation technique was used to measure the mechanical properties of the prepared films using the same Berkovich diamond probe with a tip radius of approximately 150 nm. For indentation, partial load-unload curves with 50 segments and a maximal load of 1 mN were used, as shown in Figure S2.

For the determination of elastic modulus and hardness, Oliver – Pharr's theory [36] implemented in the software Triboscan 10.0.0.1. was employed. The values in Table 2 were calculated as an average of results measured on at least 9 different places on each sample. Figure S3 presents the elastic modulus and hardness of the samples measured by the nanoindentation technique. The elastic modulus of the glass substrate was measured for comparison, and the value was 86.73 ± 10.07 GPa.

Table 2 Mechanical properties determined by nanoindentation

	Elastic modulus [GPa]	Hardness [GPa]
Glass	86.73 ± 10.07	9.19 ± 2.42
MX-5 L	89.81 ± 11.76	10.50 ± 2.70
MX-10 L	89.43 ± 21.26	7.46 ± 2.73
GO-5 L	117.98 ± 20.22	13.04 ± 3.12
GO-10 L	97.97 ± 13.45	9.80 ± 2.90

For the $Ti_3C_2T_x$ MXene samples, almost the same elastic modulus was observed, approximately 89 GPa for both films composed of 5 and 10 layers. The value was approximately 100 GPa for GO samples composed of 5 or 10 layers. In both cases, the hardness was lower for the 10-layer samples. Kariper [37] stated that there is a negative relationship between thickness and hardness, meaning that thinner films tend to be harder than thicker films. This is because thinner films have fewer grain boundaries, which can act as stress concentrators and weaken the material. Additionally, the increased strain from the indenter can more easily cause dislocations to move and plastically deform the material in thinner films. The author also provided evidence of this relationship by citing a study that found that the hardness of $Mn_2V_2O_7$ thin films decreased with increasing thickness. The study also found that the hardness of the films was correlated with the average grain size, with films with smaller grain sizes being harder than films with larger grain sizes. Finally, the author suggested that the relationship between thickness and hardness is affected by the deposition method. They stated that films deposited using sputtering tend to have a more pronounced decrease in hardness with increasing thickness than films deposited using evaporation. This is because sputtered films tend to have larger grain sizes, which can act as stress concentrators and weaken the material. The tensile test of $Ti_3C_2T_x$ films with various thicknesses (2–17 µm) prepared by he vacuum filtration showed the relative sliding between $Ti_3C_2T_x$ flakes as the dominant deformation mechanism of $Ti_3C_2T_x$ films [38]. The mechanical properties of $Ti_3C_2T_x$ films were thickness dependent. Elastic modulus decreased from 17 to 8 GPa, when the film thickness increases from 2.3 to 17 μm [38]. Overall, the author concludes that there is a complex relationship between thickness and hardness, but that thinner films tend to be harder than thicker films. These conclusions can also be observed in our results.

In the literature, the mechanical properties of GO in paper-like form or as single- or few-layer sheets are primarily reported [22, 23]. The GO paper is a self-supporting thin film that consists of aligned GO nanosheets. The ordered GO paper exhibits a wide range of elastic modulus values from 6 to 42 GPa [8]. The GO paper has a layered structure and is composed of individual, well-organized 100–200 nm thick sheets [39]. When the thickness of GO sheets decreased to a few layers, its elastic modulus increased, and values of approximately 200 GPa [24, 40] were found. In our case, the thickness of the prepared films is between the values for GO papers and GO single sheets, and the elastic modulus values are between the values for papers and single sheets.

The situation is similar to that of $Ti_3C_2T_x$ MXenes. In the existing literature, there is a greater focus on measuring the mechanical properties of monolayers of $Ti_3C_2T_x$ MXenes [13, 24]. The reported results for mechanical properties are obtained from single sheets of $Ti_3C_2T_x$ MXenes or blade coating produced films with a thickness of almost 1 µm. Such results cannot be directly compared with the measurement of sprayed layers. During spraying, the layers are randomly arranged, which can change the overall behavior and also influenced the elastic modulus of the final films. In a recent study by Wang et al. [27], the properties of $Ti_3C_2T_x$ MXene films prepared using Vacuum-Assisted Filtration (VAF) were investigated. The Young's modulus measured by Wang et al. ranged from 14 to 28 GPa. In contrast, our experimental measurements of sprayed $Ti_3C_2T_x$ MXene films yielded significantly higher Young's moduli, reaching up to 90 GPa. However, the VAF-prepared films were approximately 1,000 times thicker than the sprayed films, with thicknesses of 45 µm and 35 nm, respectively. This thickness difference is a crucial factor influencing the elastic modulus of $Ti_3C_2T_x$ MXene films, as the interlayer sliding becomes more pronounced in thicker films. The tensile strength of films fabricated through spray coating can reach up to 707 MPa, significantly higher than the 87 MPa observed in those made using vacuum-assisted filtration [25]. A single layer of $Ti_3C_2T_x$ exhibits an elastic modulus of 330 ± 30 GPa [13]. Recently, theoretical calculations predicted even higher values of the elastic modulus for different types of MXenes [41, 42]. An elastic modulus of 20.6 ± 3.1 GPa for $Ti_3C_2T_x$ films produced by blade coating was reported [43]. Our values for spray-coated films with thicknesses of approximately 36–50 nm are between these reported elastic modulus values.

Since both 2D materials in our study were prepared by comparable methods, the presented comparison of their properties is more reliable.

3.4 Contact angle measurement and surface energy calculation

To investigate the wetting properties of both the $Ti_3C_2T_x$ MXene and GO films, contact angle hysteresis measurements were performed. Surface energy was calculated using 3 liquids with different polarities - water, diiodomethane (DIO), and ethyl anthranilate (EA) (Supplement Table S1), and the Owens-Wendt method was used. Owens-Wendt is one of the most commonly used surface free energy theories. It divides the interfacial interactions into two parts: polar γ^{Pol} and dispersive γ^{Dis}.

$$\gamma_S = \gamma^{Dis} + \gamma^{Pol} \tag{2}$$

Calculation of the surface free energy with this model requires the measurement of the contact angle with at least two known liquids, and the surface energy components can be obtained by simultaneously solving two equations of the type (3).

$$\frac{\gamma_L (1 + cos\theta)}{2\sqrt{\gamma_L^{Dis}}} = \sqrt{\gamma_S^{Pol}}\sqrt{\frac{\gamma_L^{Pol}}{\gamma_L^{Dis}}} + \sqrt{\gamma_S^{Dis}} \tag{3}$$

The contact angle values used for surface energy calculations were not obtained using the common static contact angle measurement approach. This is because, on real surfaces with surface roughness and possible chemical heterogeneity, the droplet can settle in a local energy minimum within the range of contact angles, a phenomenon known as contact angle hysteresis [44]. This method has been criticized for two main reasons: (1) the reproducibility of these 'intermediate' contact angles is questionable, and (2) surface

Table 3 Advancing, receding, and most stable contact angles of water, DIO, and EG

		Θ_A (°)			Θ_R (°)			Θ_{MS} (°)	$\Theta_A - \Theta_R$ (°)
MX-5 L	DIO	50.8	±	1.2	30.8	±	3.5	41.8	20.0
	Water	59.2	±	2.7	12.9	±	1.8	42.0	46.3
	EA	27.0	±	2.1	10.1	±	1.3	20.3	16.8
MX-10 L	DIO	51.6	±	1.3	29.9	±	2.3	41.9	21.7
	Water	58.6	±	2.6	14.1	±	1.4	41.8	44.5
	EA	26.6	±	1.7	11.2	±	0.7	20.3	15.4
GO-5 L	Water	40.7	±	1.7	11.2	±	0.9	29.6	29.5
	EA	14.9	±	1.1	10.1	±	1.4	12.8	4.8
	DIO	50.5	±	0.8	27.9	±	2.0	40.5	22.5
GO-10 L	Water	38.6	±	1.8	11.4	±	0.8	28.2	27.2
	EA	14.4	±	1.0	11.6	±	0.5	13.1	2.9
	DIO	54.0	±	0.9	24.7	±	1.4	41.6	29.3

energy calculations require a contact angle corresponding to the global Gibbs free energy minimum [45]. However, direct measurement of the global Gibbs free energy minimum is feasible only in a limited number of laboratories worldwide [44, 46]. Therefore, an advancing Θ_A and receding Θ_R contact angle measurement was chosen to estimate the most stable contact angle using the approximation suggested by Andrieu et al. [47]. The advancing and receding contact angles are considered reproducible [44]. A protocol for reproducible advancing and receding contact angle measurement, which served as a guide for our measurements, was published recently [48].

$$cos\theta_{\mathrm{MS}} = \frac{cos\theta_{\mathrm{A}} + cos\theta_{\mathrm{R}}}{2} \tag{4}$$

The Young contact angle was calculated using the Wenzel equation according to the recommendation published by Marmur et al. [45, 49].

$$cos\theta_{W} = r cos\theta_{\mathrm{Y}} \tag{5}$$

The advancing and receding contact angle values, as well as the estimated equilibrium contact angle for both $Ti_3C_2T_x$ MXene and GO layers on the glass surface, are summarized in Table 3. The most stable contact angles of water on both nanomaterials calculated by formula given in Eq. (2) confirm the significant hydrophilic character for both $Ti_3C_2T_x$ MXene (41.8–41.9°) and GO (28.2–29.6°). Additionally, very small differences in contact angles were observed for 5 and 10 prepared layers, indicating a very good shielding effect, which was demonstrated previously for both $Ti_3C_2T_x$ MXene [48] and graphene [50]. The results show a giant contact angle hysteresis of water for both nanomaterials. The most common factors increasing the contact angle hysteresis are surface roughness and chemical heterogeneity [45, 46, 49]. Considering that the surface roughness ratio value remains close to 1 (see Fig. 6), there is no indication that contact angle hysteresis can be induced by surface roughness. We recently reported that for $Ti_3C_2T_x$ MXene, the contact angle hysteresis could be attributed to the chemical heterogeneity resulting from the presence of F, O, and OH terminal groups [48]. However, different functional groups (O, OH, and COOH) on the GO surface could be the main reason for such high contact angle hysteresis values of GO layers. High contact angle hysteresis for chemically heterogeneous systems has been reported previously [51–53]. Tailoring the functional groups of $Ti_3C_2T_x$ MXene significantly impacts its wettability. For example, functionalization with –OH, –O, and –F groups results in a hydrophilic surface (contact angle ~ 39°), while introducing larger, less hydrophilic groups like iodine increases the contact angle to 99°, making the surface more hydrophobic [54].

The surface energy values calculated using contact angle values from 3 different liquids (see Table 3) are listed in Table 4, including dispersive and polar parts.

Our obtained surface free energy values for GO do not differ significantly from previously reported results for thin GO films (51 mJ/m^2 [55] and 62.1 mJ/m^2 [56]). For $Ti_3C_2T_x$ MXene, the surface energy values vary in the range of 45 to 62 mJ/m^2 [48, 57, 58], and the value we determined is also in this range. These values may depend on drying and storage conditions [57], and we recently reported a possible dependence on several factors including $Ti_3C_2T_x$ MXene dispersion preparation and the quality of the preparation process or contact angle measurement approach and surface energy calculation method [48]. Since the GO surface also contains different surface functional groups, it can be

Table 4 Surface free energy components were calculated according to the OWRK model

Substrate	γ (mJ/m^2)	γ^{Dis} (mJ/m^2)	γ^{Pol} (mJ/m^2)
MX-5 L	53.18	21.77	31.41
MX-10 L	53.73	20.93	32.80
GO-5 L	61.89	19.76	42.13
GO-10 L	63.01	18.89	44.14

expected, that differences in the literature values can be due to factors affecting the surface chemistry of GO.

3.5 Electrical conductivity of $Ti_3C_2T_x$ MXene films

The sheet resistances (R_S) of the prepared samples were regularly measured by the four-point method for more than two months. The probes in this system are in one line with a spacing of 1.27 mm. We set the target current to 0.002 A, and the voltage increment was 0.01 V. The results for $Ti_3C_2T_x$ MXenes were measured because GO samples were not conductive when using this method. Sheet resistances as a mean value from 5 points were measured in each sample, and later, when the thicknesses of films (t) were calculated, sheet resistances to conductivities (σ) were recalculated with Eq. 6:

$$\sigma = \frac{1}{R_S \bullet t} \tag{6}$$

The conductivities one day after the preparation of the samples were 505 ± 80 S/cm for the 5-layer MXene film and 1086 ± 64 S/cm for the 10-layer MXene film. As reported by Y. Peng et al., electrical conductivity values were measured by a four-point probe in the range of 778–2508 S/cm, depending on the $Ti_3C_2T_x$ MXene sheet size [59]. Two main effects can have the greatest influence on conductivity: sheet-to-sheet contact resistance and defects causing more electrical resistivity.

The conductivities of the 5-layer MXene sample and 10-layer MXene sample decrease by approximately 50% and 40% after two months, respectively, as depicted in Fig. 7. Table S2 presents the results of the measurements of conductivities measured every week for two months. In our previous study, XPS and TEM in multiple modes were employed to investigate the chemical and morphological changes in 2D MXene exposed to air over a period of several months. The study revealed the progressive development of the Ti^{4+} state and the formation of TiO_2, which contributed to the gradual disintegration of 2D MXene nanosheets and the generation of additional defects. Nevertheless, the overall morphology and crystalline structure of the $Ti_3C_2T_x$ MXene nanosheets remained intact for several months [60]. Recent studies suggest that the decline in electrical conductivity is mainly due to water intercalation between hydrophilic $Ti_3C_2T_x$ MXene layers, causing partial delamination and defect formation rather than irreversible oxidation. Heating at 200 °C effectively removes interlayer water, restoring conductivity and reducing degradation. Advances in synthesis, such as minimizing chlorine terminations or residual aluminum and utilizing vacuum drying, have further enhanced $Ti_3C_2T_x$ MXene stability, with films retaining up to 90% conductivity after 5 years of storage [61].

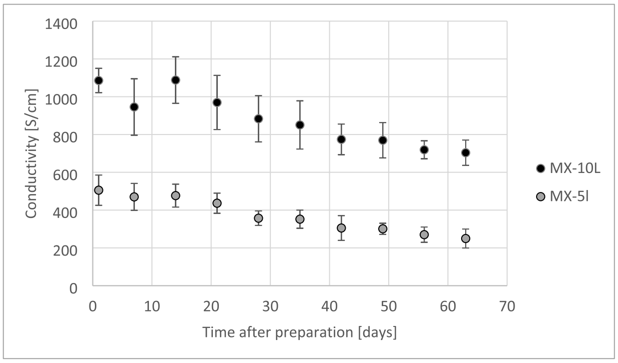

Fig. 7 Time dependence of the conductivity of $Ti_3C_2T_x$ MXene samples

4 Conclusions

The spray coating method proved to be an efficient and versatile approach for fabricating thin, uniform, and mechanically stable $Ti_3C_2T_x$ MXene and GO films. Both materials exhibited comparable mechanical properties (elastic modulus ~ 89 GPa for $Ti_3C_2T_x$ MXene and ~ 100 GPa for GO) and hydrophilic character, with contact angles between 28.2° and 41.9°. SPM imaging confirmed homogeneous surface coverage, and film thicknesses ranged from ~ 23 to 50 nm, corresponding to 18–40 monolayers based on XRD analysis.

Surface energy values (45–62 mJ/m² for $Ti_3C_2T_x$ MXene, 51–62 mJ/m² for GO) suggest similar affinities to polar environments. Despite minor oxidation and fluorine terminations observed in $Ti_3C_2T_x$ MXene (confirmed by XPS), films exhibited good chemical quality. GO films showed characteristic peaks (284–289 eV) consistent with high purity.

Electrical conductivity reached 505 S/cm (5 layers) and 1086 S/cm (10 layers) in $Ti_3C_2T_x$ MXene films but dropped by ~ 50% and ~ 40%, respectively, after two months due to oxidation. These findings underscore the need for optimized storage—e.g. inert atmosphere or refrigeration—and the potential use of protective polymer layers for stability in ambient conditions.

This study offers the first direct comparison of $Ti_3C_2T_x$ MXene and GO films produced under identical spray coating conditions, providing new insights into their structural, mechanical, and surface properties. Developing strategies to mitigate $Ti_3C_2T_x$ MXene oxidation is crucial for realizing the full potential of these materials in various applications. This may involve capping agents or protective coatings to prevent oxygen exposure and maintain their electrical conductivity.

Supplementary Information The online version contains supplementary material available at https://doi.org/10.1007/s42247-025-01215-4.

Acknowledgements This work was supported by Slovak Grant Agency, projects APVV 19–0465 and project VEGA 2/0006/22. We greatly appreciate Dr. A. Šiskova for the SEM study and Dr. M. Jergel for XRD investigation.

Author contributions All authors contributed to the study conception and design. Material preparation, data collection, and analysis were performed by Michal Procházka, Yaryna Soyka (resources, investigation), Anastasiia Stepura (methodology, investigation), Nikola Bugárová (resources, investigation), Peter Machata (methodology, visualization, investigation), Matej Mičušík (methodology, investigation), Gediminas Monastyreckis (formal analysis, investigation), and Daiva Zeleniakiene (validation, investigation). The first draft of the manuscript was written by Michal Procházka (conceptualization, writing – original draft, methodology, investigation) and all authors commented on previous versions of the manuscript. Andrey Aniskevich (conceptualization, writing – review & editing) and Mária Omastová (conceptualization, writing – review & editing, supervision, funding acquisition) also contributed to the manuscript revision. All authors read and approved the final manuscript.

Funding Open access funding provided by The Ministry of Education, Science, Research and Sport of the Slovak Republic in cooperation with Centre for Scientific and Technical Information of the Slovak Republic.

Data availability The authors declare that the data supporting the findings of this study are available within the paper and its Supplementary Information files. Should any raw data files be needed in another format they are available from the corresponding author upon reasonable request.

Declarations

Competing interest The authors declare that they have no known competing financial interests or personal relationships that could have appeared to influence the work reported in this paper.

References

1. G. Cao, H. Gao, Prog Mater. Sci. **103** (2019). https://doi.org/10.1016/j.pmatsci.2019.03.002
2. A.K. Geim, Phys. Scr. (2012). https://doi.org/10.1088/0031-8949/2012/T146/014003
3. W.S. Hummers, R.E. Offeman, J. Am. Chem. Soc. **80**, 6 (1958). https://doi.org/10.1021/ja01539a017
4. E. Aliyev, V. Filiz, M.M. Khan, Y.J. Lee, C. Abetz, V. Abetz, Nanomaterials. **9**, 8 (2019). https://doi.org/10.3390/nano9081180
5. M.Q. Zhao, C.E. Ren, Z. Ling, M.R. Lukatskaya, C. Zhang, K.L. Van Aken, M.W. Barsoum, Y. Gogotsi, Adv. Mater. **27**, 2 (2015). https://doi.org/10.1002/adma.201404140
6. Z. Zhang, H.C. Schniepp, D.H. Adamson, N.Y. Carbon, (2019) https://doi.org/10.1016/j.carbon.2019.07.103
7. R. Al-Gaashani, A. Najjar, Y. Zakaria, S. Mansour, M.A. Atieh, Ceram. Int. **45**, 11 (2019). https://doi.org/10.1016/j.ceramint.2019.04.165
8. E. Alejandra Huitrón, D. Segovia, J. Torres- Torres, A. Raúl Pérez Higareda, García-García, Mech. Mater. **158** (2021). https://doi.org/10.1016/j.mechmat.2021.103875
9. H. Kim, Y. Miura, C.W. MacOsko, Chem. Mater. **22** (2010). 11https://doi.org/10.1021/cm100477v
10. S. Park, J. An, R.D. Piner, I. Jung, D. Yang, A. Velamakanni, S.B.T. Nguyen, R.S. Ruoff, Chem. Mater. **20**, 21 (2008). https://doi.org/10.1021/cm801932u
11. M. Naguib, M. Kurtoglu, V. Presser, J. Lu, J. Niu, M. Heon, L. Hultman, Y. Gogotsi, M.W. Barsoum, Adv. Mater. **23**, 37 (2011). https://doi.org/10.1002/adma.201102306
12. B. Anasori, Y. Xie, M. Beidaghi, J. Lu, B.C. Hosler, L. Hultman, P.R.C. Kent, Y. Gogotsi, M.W. Barsoum, ACS Nano. **9**, 10 (2015). https://doi.org/10.1021/acsnano.5b03591
13. A. Lipatov, H. Lu, M. Alhabeb, B. Anasori, A. Gruverman, Y. Gogotsi, A. Sinitskii, Sci. Adv. **4**, 6 (2018). https://doi.org/10.1126/sciadv.aat0491
14. S. Wang, Y. Liu, Y. Liu, Z. Shi, J. Zhou, J. Zhu, W. Hu, Cell. Rep. Phys. Sci. **3**, 11 (2022). https://doi.org/10.1016/j.xcrp.2022.101151
15. J. Zhang, S. Li, S. Hu, Y. Zhou, Materials. **11**, 10 (2018). https://doi.org/10.3390/ma11101979
16. A.C.Y. Yuen, T.B.Y. Chen, B. Lin, W. Yang, I.I. Kabir, I.M. De Cachinho Cordeiro, A.E. Whitten, J. Mata, B. Yu, H.-D.D. Lu, G.H. Yeoh, Compos. Part. C: Open. Access. **5** (2021). https://doi.org/10.1016/j.jcomc.2021.100155
17. L.Å. Näslund, I. Persson, Appl. Surf. Sci. **593** (2022). https://doi.org/10.1016/j.apsusc.2022.153442
18. D. Zeleniakiene, G. Monastyreckis, A. Aniskevich, P. Griskevicius, Materials. **13**, 5 (2020). https://doi.org/10.3390/ma13051253
19. A. Lipatov, A. Goad, M.J. Loes, N.S. Vorobeva, J. Abourahma, Y. Gogotsi, A. Sinitskii, Matter. **4**, 4 (2021). https://doi.org/10.1016/j.matt.2021.01.021
20. Z. Ling, C.E. Ren, M.-Q. Zhao, J. Yang, J.M. Giammarco, J. Qiu, M.W. Barsoum, Y. Gogotsi, Proc. Natl. Acad. Sci. U. S. A. (2014). https://doi.org/10.1073/pnas.1414215111
21. S. Tarasovs, A. Aniskevich, Mech. Mater. **167** (2022). https://doi.org/10.1016/j.mechmat.2022.104247
22. A.R. Khoei, M.S. Khorrami, Fullerenes, Nanotubes Carbon Nanostruct. **24**, 9 (2016). https://doi.org/10.1080/1536383X.2016.1208180
23. L. Liu, J. Zhang, J. Zhao, F. Liu, Nanoscale. **4**, 19 (2012). https://doi.org/10.1039/c2nr31164j
24. J.W. Suk, R.D. Piner, J. An, R.S. Ruoff, ACS Nano. **4**, 11 (2010). https://doi.org/10.1021/nn101781v
25. A. Kamal, B. Li, S. Luo, I. Kinloch, L. Zheng, K. Liao, Nano Mater. Sci. (2025). https://doi.org/10.1016/j.nanoms.2025.03.006
26. S. Anwer, B. Li, S. Luo, T. Alkhidir, S. Mohamed, V. Chan, K. Liao, J. Micromech Mol. Phys. **06**, 03 (2021). https://doi.org/10.1142/S2424913021430049
27. J. Wang, J. He, D. Kan, K. Chen, M. Song, W. Huo, Cryst. (Basel). **12**, 8 (2022). https://doi.org/10.3390/cryst12081034

28. R. Indhumathi, A.S. Priya, R. Aepuru, K. Shanmugaraj, J. Mater. Sci. **60**, 13 (2025). https://doi.org/10.1007/s10853-025-10728-6
29. J. Karthikeyan, The cold spray materials deposition process. Elsevier. 62–71 (2007)
30. M. Alhabeb, K. Maleski, B. Anasori, P. Lelyukh, L. Clark, S. Sin, Y. Gogotsi, Chem. Mater. **29**, 18 (2017). https://doi.org/10.1021/acs.chemmater.7b02847
31. M. Malaki, A. Maleki, R.S. Varma, J. Mater. Chem. Mater. **7**, 18 (2019). https://doi.org/10.1039/C9TA01850F
32. X. Sang, Y. Xie, M.-W. Lin, M. Alhabeb, K.L. Van Aken, Y. Gogotsi, P.R.C. Kent, K. Xiao, R.R. Unocic, ACS Nano. **10**, 10 (2016). https://doi.org/10.1021/acsnano.6b05240
33. N. Bugárová, Z. Špitálsky, M. Mičušík, M. Bodík, P. Šiffalovič, M. Koneracká, V. Závišová, M. Kubovčíková, I. Kajanová, M. Zaťovičová, S. Pastoreková, M. Šlouf, E. Majková, M. Omastová, Cancers (Basel). **11**, 6 (2019). https://doi.org/10.3390/cancers11060753
34. D.C. Marcano, D.V. Kosynkin, J.M. Berlin, A. Sinitskii, Z. Sun, A. Slesarev, L.B. Alemany, W. Lu, J.M. Tour, ACS Nano. **4**, 8 (2010). https://doi.org/10.1021/nn1006368
35. T. Bu, H. Gao, Y. Yao, J. Wang, A.J. Pollard, E.J. Legge, C.A. Clifford, A. Delvallée, S. Ducourtieux, M.A. Lawn, B. Babic, V.A. Coleman, Å. Jämting, S. Zou, M. Chen, Z.J. Jakubek, E. Iacob, N. Chanthawong, K. Mongkolsuttirat, G. Zeng, C.M. Almeida, B.-C. He, L. Hyde, L. Ren, Nanotechnology. **34**, 22 (2023). https://doi.org/10.1088/1361-6528/acbf58
36. W.C. Oliver, G.M. Pharr, J. Mater. Res. **19**, 1 (2004). https://doi.org/10.1557/jmr.2004.19.1.3
37. I.A. Kariper, Diamond and carbon composites and nanocomposites. InTech. (2016)
38. S. Luo, S. Patole, S. Anwer, B. Li, T. Delclos, O. Gogotsi, V. Zahorodna, V. Balitskyi, K. Liao, Nanotechnology. **31**, 39 (2020). https://doi.org/10.1088/1361-6528/ab94dd
39. Z.U. Khan, A. Kausar, H. Ullah, A. Badshah, W.U. Khan, J. Plast. Film Sheeting. **32**, 4 (2016). https://doi.org/10.1177/8756087915614612
40. J.T. Robinson, M. Zalalutdinov, J.W. Baldwin, E.S. Snow, Z. Wei, P. Sheehan, B.H. Houston, Nano Lett. **8**, 10 (2008). https://doi.org/10.1021/nl8023092
41. Y. Ibrahim, A. Mohamed, A.M. Abdelgawad, K. Eid, A.M. Abdullah, A. Elzatahry, Nanomaterials. **10**, 10 (2020). https://doi.org/10.3390/nano10101916
42. G. Plummer, B. Anasori, Y. Gogotsi, G.J. Tucker, Comput. Mater. Sci. **157** (2019). https://doi.org/10.1016/j.commatsci.2018.10.033
43. V. Kedambaimoole, K. Harsh, K. Rajanna, P. Sen, M.M. Nayak, S. Kumar, Mater. Adv. **3**, 9 (2022). https://doi.org/10.1039/D1MA01170G
44. T. Huhtamäki, X. Tian, J.T. Korhonen, R.H.A. Ras, Nat. Protoc. **13**, 7 (2018). https://doi.org/10.1038/s41596-018-0003-z
45. A. Marmur, Annu. Rev. Mater. Res. (2009). https://doi.org/10.1146/annurev.matsci.38.060407.132425
46. J.W. Drelich, Adv. Colloid Interface Sci. (2019). https://doi.org/10.1016/j.cis.2019.02.002
47. C. Andrieu, C. Sykes, F. Brochard, Langmuir (1994). https://doi.org/10.1021/la00019a010
48. P. Machata, M. Hofbauerová, Y. Soyka, A. Stepura, D. Truchan, Y. Halahovets, M. Mičušík, P. Šiffalovič, E. Majková, M. Omastová, J. Colloid Interface Sci. **622** (2022). https://doi.org/10.1016/j.jcis.2022.04.135
49. A. Marmur, Contact Angle, Wettability and Adhesion. Brill Academic. **6**, 1–18 (2010)
50. R. Raj, S.C. Maroo, E.N. Wang, Nano Lett. **13**, 4 (2013). https://doi.org/10.1021/nl304647t
51. L.W. Schwartz, S. Garoff, Langmuir 1, 2 (1985) https://doi.org/10.1021/la00062a007
52. R.H. Dettre, R.E. Johnson, J. Phys. Chem. **69**, 5 (1965). https://doi.org/10.1021/j100889a012
53. J. Drelich, Pol. J. Chem. **71**, 5 (1997)
54. M. Hilal, W. Yang, Y. Hwang, W. Xie, Nanomicro Lett. **16**, 1 (2024). https://doi.org/10.1007/s40820-023-01316-x
55. F. Perrozzi, S. Croce, E. Treossi, V. Palermo, S. Santucci, G. Fioravanti, L. Ottaviano, Carbon N Y. **77** (2014). https://doi.org/10.1016/j.carbon.2014.05.052
56. S. Wang, Y. Zhang, N. Abidi, L. Cabrales, Langmuir. **25**, 18 (2009). https://doi.org/10.1021/la901402f
57. H. Zhou, F. Wang, Y. Wang, C. Li, C. Shi, Y. Liu, Z. Ling, RSC Adv. **11**, 10 (2021). https://doi.org/10.1039/D0RA09125A
58. K. Zukiene, G. Monastyreckis, S. Kilikevicius, M. Procházka, M. Micusik, M. Omastová, A. Aniskevich, D. Zeleniakiene, Mater. Chem. Phys. **257** (2021). https://doi.org/10.1016/j.matchemphys.2020.123820
59. Y.-Y. Peng, B. Akuzum, N. Kurra, M.-Q. Zhao, M. Alhabeb, B. Anasori, E.C. Kumbur, H.N. Alshareef, M.-D. Ger, Y. Gogotsi, Energy Environ. Sci. **9**, 9 (2016). https://doi.org/10.1039/C6EE01717G
60. M. Mičušík, M. Šlouf, A. Stepura, Y. Soyka, E. Ovodok, M. Procházka, M. Omastová, Appl. Surf. Sci. **610** (2023). https://doi.org/10.1016/j.apsusc.2022.155351
61. A. Lee, M. Shekhirev, M. Anayee, Y. Gogotsi, Graphene 2D Mater. **9**, 1–2 (2024). https://doi.org/10.1007/s41127-024-00076-8

Highlights

- The challenge of characterizing the physical properties of 2D materials was addressed.
- Two types of 2D materials, graphene oxide and $Ti_3C_2T_x$ MXene, were analyzed and compared.
- The main differences were caused by sample type, not by sample thickness.